BNL-77943-2007-BC

Electron Holography of Electromagnetic Fields: Recent Theoretical Advances

M. Beleggia[1], G. Pozzi[2], A. Tonomura[3,4]

[1] *Brookhaven National Laboratory, Building 480, Upton, NY 11973, USA*

[2] *University of Bologna, Viale B. Pichat 6/2, 40127 Bologna, Italy*

[3] *Frontier Research System, the Institute of Physical and Chemical Research (RIKEN), Hirosawa, Wako, Saitama 351-0198, Japan*

[4] *Advanced Research Laboratory, Hitachi Ltd., Akanuma, Hatoyama, Saitama 350-0395, Japan*

To be published in "Introduction to Electron Holography, Volume 2"

April 2007

Center for Functional Nanomaterials

Brookhaven National Laboratory
P.O. Box 5000
Upton, NY 11973-5000
www.bnl.gov

DISCLAIMER

BNL-77943-2007-BC

Electron holography of electromagnetic fields: recent theoretical advances

M. Beleggia[1], G. Pozzi[2], A. Tonomura[3,4]

[1] *Brookhaven National Laboratory, Building 480, Upton, NY 11973, USA*

[2] *University of Bologna, Viale B. Pichat 6/2, 40127 Bologna, Italy*

[3] *Frontier Research System, the Institute of Physical and Chemical Research (RIKEN), Hirosawa, Wako, Saitama 351-0198, Japan*

[4] *Advanced Research Laboratory, Hitachi Ltd., Akanuma, Hatoyama, Saitama 350-0395, Japan*

April 16, 2007

1 Introduction

Since the first edition of this book was published, research involving electron holography and its applications to the investigation of electromagnetic fields has made substantial progress, both from the experimental and theoretical points of view. An influential driving force in this direction has been the interest in dynamical observations of superconducting vortices in conventional and high-T_c materials using the Fresnel (out-of-focus) method of Lorentz microscopy. In fact, owing to the large London penetration depth λ_L typical of high-T_c superconductors, the need to observe specimens with a thickness comparable or even larger than λ_L in order to obtain reliable information on the vortex core structure has prompted the development of a high voltage (1 MV) electron holography microscope [1, 2]. This instrument, equipped with two electron biprisms, enables us to explore and develop new modes of electron interferometry and holography, where fringe spacing and orientation, as well as field of view, can be independently controlled [4, 5, 6].

On the other hand, observations of flux line lattices and pancake vortices in anisotropic and layered superconductors revealed the inadequacy of the real space approach based on the flux tube model to cope with such structures, and prompted us to develop a more powerful and general Fourier space approach. This chapter is devoted primarily to a general review of Fourier methods for computing electron-optical phase shifts associated to electric and/or magnetic fields. The phase shift, in fact, represents the link connecting electron holography experiments and the physics of materials, structures and devices under study in a transmission electron microscope. A link that can be followed through and exploited properly only when a physically sound model is available for the interpretation of the phase modulation retrieved from the experiments.

In this chapter, we will first present an overview of the early steps which led us to the development of the Fourier approach to phase computations. In chapter 7 of Ref. [7] [**reference to first edition, to be updated and/or adjusted as appropriate**], we introduced the simple model associated to a flux tube, an elementary quantized vortex where the singular magnetic field is concentrated in a region of negligible radius. The phase shift associated with a flux tube can be computed analytically in real space, and represented a milestone towards the development of realistic models. In fact, by convoluting it with a suitable magnetic field distribution, it has been possible to obtain realistic simulations that contributed to the interpretation of the very first results obtained by electron holography on vortex matter [8, 9, 10]. The next step, illustrated in section 2, was to realize that in order to calculate the total phase shift associated to a vortex lattice, it was necessary to evaluate the Fourier transform of the single fluxon phase, and sample it over the reciprocal lattice. This idea led to remarkable computational benefits, as it enabled us to simulate lattices at small or large magnetic fields (the lattice spacing is inversely proportional to the applied field), and interpret Foucault and Fresnel observations of vortex matter. In section 3, we review the extension of the theoretical framework leading to the computation of fields and phase shifts associated to vortices in anisotropic materials. This extension was particularly useful to interpret experiments on high-T_c materials, especially YBCO, and to demonstrate the capability of Fresnel methods and electron holography to distinguish between pinned and unpinned vortices by examining the fine features of the image contrast or phase shifts respectively. In section 4, we examine the problem of layered materials, with highly anisotropic materials such as BSCCO in mind, where vortices have

an instrinsic two-dimensional structure imposed by the supercurrents flowing only within the CuO planes. The main benefit of this extension was the opportunity to simulate more exotic structures, such as kinked vortices occurring when the external field is applied at large angles with respect to the sample perpendicular direction. Simulation of the phase shift associated with Josephson vortices is also possible, but since no experimental evidence is yet present in the literature, we choose not to discuss the issue here and refer the reader to Ref. [11].

While our work was initially motivated by our ongoing research on superconducting vortices, the usefulness of the obtained results prompted us to apply Fourier methods in other directions. In particular, the analysis of electrostatic fields associated to reverse-biased p-n junctions, reviewed in section 5, of magnetic fields produced by stripe domains near the sample edge, section 6, and finally of magnetic nanoparticles with various shapes, section 7. In all these cases the Fourier method enabled us to produce a wealth of unexpected and useful results, very often in analytical form, which makes this approach invaluable in the theoretical investigation of long range electromagnetic fields as observed and measured by electron holography and microscopy.

2 From the isolated vortex to the flux line lattice case

After the first successful observations of superconducting vortices or fluxons by means of the Fresnel and holography techniques [8, 9, 10], other Lorentz microscopy phase contrast methods have been applied, and low angle electron diffraction and Foucault experiments have been carried out on superconducting specimens in a range of applied magnetic fields where vortices are arranged over a more or less regular lattice [12, 13]. In order to interpret these results, we started from the flux tube model and we approximated the fluxon by a suitable bundle of straight flux tubes, relying on the important result that the phase shift of the flux tube can be calculated analytically even in the tilted specimen geometry [10, 14]. In this way, by convolving this elementary phase shift with a chosen projected magnetic field distribution, we obtain a fairly realistic model capable of describing satisfactorily the main features of experimental results.

We considered the case of a London bulk model [15], in which the magnetic field is described by the following equation,

$$B = \frac{\Phi_0}{2\pi r_F^2} K_0 \left(\frac{r}{r_F} \right) \tag{1}$$

where $\Phi_0 = h/(2e) = 2.07 \times 10^{-15}$ T m^2 is the flux quantum (h being the Planck constant and e the absolute value of the electron charge), K_0 is the zero-order modified Bessel function, r the radial distance from the vortex axis and r_F a phenomenological parameter linked to the vortex radius, of the same order of magnitude as the London penetration depth. For thin films of conventional superconductors like Niobium, where $\lambda_L \sim 30$ nm and the film thickness is about t=60 nm, the value r_F= 50 nm gives results in good agreement with the experimental findings [16]. For the sake of generality, and for an easy extension of the results to other materials, we have kept all the distances expressed in unit of r_F. Therefore, in order to simulate a fluxon lattice, we started with the idea of taking a large but finite array of fluxons, calculating the phase shift and selecting the central part of the region. Figure 1(a) reports the results obtained for the case of an ideal triangular lattice of spacing $s = \sqrt{2\Phi_0/(\sqrt{3}B)}$=$6r_F$=300 nm corresponding to an applied field perpendicular to the sample surface of B=37.5 mT. Note that in actual experiments the field is tilted at 45° with respect to the specimen normal. The number of fluxons used in this computation is 331, and only the central region, a square of side $20r_F$=1 μm, containing about 20 fluxons, is shown.

The surface plot of the phase shift, to which a linear term has been subtracted, clearly shows the hills and valleys associated to each fluxon. Note also that the triangular lattice is distorted owing to its projection onto the observation plane. Figure 1(b) displays the surface plot of the phase when the lattice spacing is reduced to s=150 nm=$3r_F$. The number of fluxons is still 331 as in Fig.1(a), whereas in Fig.1(c) and (d) it has been increased to 1261 and 4921 fluxons respectively. These values stem from the fact that we surrounded the central region of $20r_F$ by an increasing number of hexagonal shells along the external perimeter.

When the lattice parameter is not too small, as in Fig.1(a), the finite sum of single fluxons gives good results, while if we decrease the lattice spacing we notice a large residual curvature of the phase, even when the linear contribution is subtracted, as shown in Fig.1(b). This curvature can be reduced by increasing the fluxon number, Fig.1(c), but it is still detectable even for

the largest value, Fig.1(d). This is due to the long range behaviour of the flux tube phase, which depends on the angle and not on the distance from the fluxon. As a consequence, a very large number of fluxons is needed in order to smooth the phase and approximate the periodic case. It is therefore clear that the idea of taking a large but finite array of fluxons, calculating the phase shift and selecting the basic unit cell in the central part of the region, and then computing the various images by Fourier methods by periodic prolongation is not a very efficient procedure, as it leads quickly to unmanageable computing times and memory requirements.

These effects are particularly important in the case of high-T_c superconductors, where penetration depth and fluxon radius are of the order of 200-400 nm respectively, so that highly packed lattices with overlapping fields are the standard. On the other hand, in these conditions where the phase presents only a slight modulation with respect to its average value, only a relatively small number of Fourier coefficients is needed. Therefore, the availability of the phase shift in Fourier representation could lead to a substantial gain in computing time and accuracy. For these reasons, the problem of computing the Fourier coefficients of the phase has been reconsidered, and solved, using a completely different approach, where first the vector potential of the magnetic field is solved in Fourier space and decomposed into Fourier components, and then the phase shift is calculated for each component separately [17, 18]. In this way the Fourier transform of the phase shift is immediately obtained, and can be inverted either analytically or numerically.

For the case of the flux tube, this procedure leads to the following result for the phase shift in Fourier space

$$\tilde{\varphi}(k_x, k_y) = -2\pi i \frac{k_y}{k_\perp^2} \left[\frac{\sin(ak_x)}{k_x} + \frac{\sin\alpha \cos(ak_x)}{\sqrt{k_x^2 \cos^2\alpha + k_y^2}} \right] \tag{2}$$

with $k_\perp = \sqrt{k_x^2 + k_y^2}$. The equivalence of the Fourier and real space representations can be proved by direct computation [17].

As mentioned before, the London model provides a fairly reasonable description of the field in high-T_c materials. The necessary convolution with the flux tube is conveniently performed in the Fourier space by multiplying $\tilde{\varphi}$ and $\tilde{B}$, the Fourier transform of the projected field. As the expression of $\tilde{B}$ can be easily calculated by means of tables of integrals [19]

$$\tilde{B}(k_x, k_y) = \frac{\Phi_0}{1 + r_F^2(k_x^2 \cos^2\alpha + k_y^2)} \tag{3}$$

we arrive at the important result that the Fourier transform $\tilde{\phi}(k_x, k_y)$ of a fluxon described by the London field topography is known analytically. Let us assume that the fluxons are arranged over a two-dimensional Bravais lattice, having basis vectors projected in the object plane given by $\mathbf{a}_1 = (a_{11}, a_{12})$ and $\mathbf{a}_2 = (a_{21}, a_{22})$. In this way, it is possible to locate each fluxon of the lattice by means of its Bravais vector $\mathbf{r}_{n,m} = n\mathbf{a}_1 + m\mathbf{a}_2$, where n and m are integers. The lattice phase $\phi_{lat}(x, y)$ can be expressed as:

$$\phi_{lat}(\mathbf{r}) = \sum_{n,m=-\infty}^{+\infty} \phi(\mathbf{r} - \mathbf{r}_{n,m}) = \phi(\mathbf{r}) *^2 \mathrm{III}(\mathbf{r}) \tag{4}$$

where the symbol $*$ represents the convolution and the function ${}^2\mathrm{III}(\mathbf{r})$ is a two-dimensional array of Dirac delta functions (bed-of-nails or shah function [20]) centered on the lattice sites:

$${}^2\mathrm{III}(\mathbf{r}) = \sum_{n,m=-\infty}^{+\infty} {}^2\delta(\mathbf{r} - \mathbf{r}_{n,m}) \tag{5}$$

Formally exploiting the convolution theorem, we can again express the FT of the lattice phase as the product

$$\tilde{\phi}_{lat} = \tilde{\phi} \cdot {}^2\tilde{\mathrm{III}} = \tilde{\varphi} \cdot \tilde{B} \cdot {}^2\tilde{\mathrm{III}} \tag{6}$$

in which all the terms are known. In fact the FT of the function ${}^2\mathrm{III}(\mathbf{r})$ is another two-dimensional shah function, with the delta functions now centered on the reciprocal lattice sites $\mathbf{k}_{n,m}$

$${}^2\mathrm{III}(p, q) = C \sum_{n,m=-\infty}^{+\infty} {}^2\delta(\mathbf{k} - \mathbf{k}_{n,m}) \tag{7}$$

with a normalization factor C given by:

$$C^{-1} = \begin{vmatrix} a_{11} & a_{12} \\ a_{21} & a_{22} \end{vmatrix} \tag{8}$$

Going back to the lattice phase, we obtain:

$$\phi_{lat}(\mathbf{r}) = C \int e^{2\pi i \mathbf{r}\cdot\mathbf{k}} \tilde{\phi}(\mathbf{k}) \sum_{n,m=-\infty}^{+\infty} {}^2\delta(\mathbf{k} - \mathbf{k}_{n,m}) \mathrm{d}\mathbf{k} = \tag{9}$$

$$= C \sum_{n,m=-\infty}^{+\infty} \tilde{\phi}(\mathbf{k}_{n,m}) e^{2\pi i \mathbf{r}\cdot\mathbf{k}_{n,m}} \tag{10}$$

which is the expression needed for computing the simulations for the periodic case. This expression shows that the value of the phase spectrum at the reciprocal lattice sites plays the role of Fourier coefficient of the lattice phase described as a Fourier series. This infinite series can be truncated as soon as the spectrum reaches a value low enough to insure the precision we want to achieve. It can be ascertained, by calculating the phase for some ideal lattices, that taking small lattice parameters, i.e. large reciprocal lattice vectors, helps the convergence, thus obtaining the opposite result, in terms of computation times, than with the previous approach: the more packed the lattice is, the shorter and more accurate is the calculation. This is due to the fact that when the fluxons are very close to each other, the only effect that they have on the electron beam is a slight modulation of the wave front, so that a Fourier series with very few coefficients is required to reproduce it. Figure 2(a) reports the three-dimensional phase plot calculated for the same data as Fig.1(a), taking $|m, n| \leq 12$, Figure 2(b) the plot calculated for the data of Fig.1(b) with $|m, n| \leq 8$, whereas Figure 2(c) shows the results obtained when the lattice spacing equals r_F=50 nm with $|m, n| \leq 8$ (higher Fourier terms are uninfluential). We note that this simulation is beyond our present computing capabilities if the single fluxon approach is followed.

3 From London to anisotropic vortices

It was soon realized that this new approach to the calculation of the phase shift could be profitably extended to cope with situations treatable only approximatively in real space. In particular, the analytical solution in the Fourier space of a London fluxon in a thin film taking into account the effects of the surfaces has been found [18] and compared with the previous approximate one [21] where, relying on the straight flux tube model, the magnetic field within the specimen was assumed to be constant and equal to its value at the surfaces. We have also confirmed the substantial correctness of the earlier error estimate made by resorting to a parabolic approximation for the trend of the field lines within the specimen [21].

However, more interesting results have been obtained by applying the Fourier approach to models which are suggested by experiments [22], where superconducting specimens irradiated with heavy ions in a direction different

from the normal have been studied in order to directly observe the pinning of the vortices at columnar defects. In particular, the first analysis of the contrast features strongly suggested that anisotropy plays an important role in determining the outcome of transmission electron microscopy experiments [23] so that we have investigated the model of a tilted London vortex in a thin anisotropic slab.

Again, the analytical solution of this problem has been obtained in the Fourier approach [24] and Fig.3 shows the phase maps calculated in the three ortogonal directions (x_S,y_S,z_S) for a vortex laying on the columnar defect which is tilted at and angle $\theta = 45°$ with respect to the specimen normal (z_S axis). The projected view of the columnar defect is indicated by the short bold line (white in Figure 3(c)) in the plots. The first three plots (a,b,c) correspond to an isotropic material with $\gamma = 1$ (γ is the anisotropy parameter, defined as the ratio between λ_c and λ_{ab}, i.e. $\gamma = \lambda_c/\lambda_{ab}$), while the last one (d) to a medium anisotropic material with $\gamma = 5$. In the x_S and y_S projections, no visible difference can be appreciated between the plots corresponding to different values of γ. This is because when we calculate the phase shift in the x_S or y_S direction, the only significant contribution comes from the tangential components of the vector potential, which are independent on λ_c. Therefore, the isotropic and anisotropic cases are identical in this case and only one example, the isotropic case, is reported. On the contrary, the second row reports a striking difference between the two cases examined. Each contour line represents a phase shift of 10 mrad, and when the anisotropy parameter γ is increased, the phase shift decreases drastically, as can be seen in the last plot, Fig. 3(d). It can be ascertained that increasing furthermore the value of γ (in real materials it can be equal to 200 or more), the phase shift is in the order of some μrads, well below the detectability limit of $\pi/100 \simeq 30$ mrad [25].

The following Fig. 4 shows a series of out-of-focus and holographic images calculated for increasing γ values, from 1 to infinity (corresponding to the pancake model: see next section 4), for a vortex core pinned at a columnar defect tilted at $\theta = 45°$ with respect the specimen normal and rotated of $\beta = 90°$ around it. Analyzing the progressive disappearence of the apparent vortex tilt with increasing anisotropy, the conclusion can be drawn that these phase contrast techniques are enough sensitive on the variation of γ when the parameter is close to the unity, but they predict almost indistinguishable images when $\gamma > 10$ [23]. The agreement with the experimental results [23, 24] is excellent and confirms the role played by anisotropy in affecting

the phase contrast images of pinned vortices.

4 Pancake vortices

One of the most striking features of vortices in layered high-T_c superconductors (for reviews see, e.g., [26, 27]) is that they can be arranged in pancake structures [28] where the layer coupling is, for highly anisotropic materials, mainly due to the magnetic field between them. As emphasized in Ref. [29] this system is qualitatively different from the bulk superconductor, as there is no phase coherence across the layers. Therefore, whereas in three-dimensional bulk materials, the fluxons are prohibited from terminating inside the material because of topology (the phase changes by 2π when the vortex core at which the phase is singular is encircled), this restriction is no longer valid in layered systems with no Josephson coupling. A vortex perpendicular to the layers can terminate at any one of them and channel the flux, at least partially, into the interlayer space. It has been argued in [29] that such termination may be energetically favourable in specimens of finite size. It is therefore exciting to model these structures and ascertain whether they can be detected by transmission electron microscopy phase contrast/retrieval techniques. As a first step, we have solved the problem of the Pearl vortex in a thin film and extended it to the three layers case [18]. Then the case of a stack of thin layers has been considered, as it can mimic well the structure of highly anisotropic superconductors [24]. Unfortunately, the number of layers dictated by the algebric approach followed was limited to seven, a rather small number to be truly representative of the actual specimen where the layers may easily be several hundreds. Nonetheless, the contour line maps of the projected magnetic field showed a strong overall similarity with the continuous anisotropic case (see below) and also the out-of-focus images calculated for vortices pinned at tilted columnar defects showed no significant differences [24].

Further experiments carried out with applied magnetic field tilted at a very large angle with respect to the specimen surfaces [30] showed new interesting features in the out-of-focus images. By increasing the applied field angle the vortex cores become first elongated as if they were following (with some lag) the direction of the field and then, at the largest angle, sometimes exhibit a dumbbell-like appearance. These observations indicate that something peculiar is happening to the vortex structure. Unfortunately these

features cannot be interpreted on the basis of the models described so far. In fact, in the continuous-anisotropic model the vortex core is straight, and with the pancake model at such large angles the small number of layers becomes visible in the image, introducing unwanted artifacts.

In order to develop a more flexible model, two options are available: deforming the core in the continuous-anisotropic model, or giving suitable coordinates for the location of each pancake in the stack. While the first turns out to be very cumbersome, the second is more practicable, provided the number of layers is increased. For this purpose, we followed the approach proposed by Clem [31, 32] and further developed by Coffey and Phipps [33], who replaced all the screening layers above and below the layer containing the vortex with a superconducting continuum that carries supercurrents parallel to the layers. In this way the algebraic troubles linked to the increasing number of unknowns arising in the former approach are circumvented and an analytical expression for the field and phase shift for the single pancake has been obtained [34]. Then, from the solution, more representative or exotic vortex structures can be investigated by adding suitably placed pancakes over a larger number of layers.

It is worthwhile to compare the semi-continuous approach with the previous one [24]. A 75° tilted stack of pancake vortices, aligned to a row of pinning centers piercing the specimen at the same angle, is shown in Fig.5. The overall similarity between the two cases is clearly displayed, with small differences detectable in the curvature of the projected field lines between the layers, due to the larger magnetic screening power of the superconducting regions with respect to vacuum areas. Such differences, however, are hardly detectable in the out-of-focus images due to the feature-broadening effect typical of the Fresnel technique.

However, when the stack tilt angle is increased up to 85°, artifacts are introduced: as visible in the contour line map and in the out-of-focus images, the single pancakes can be clearly distinguished [34]. If we increase the number of pancakes to 15, something possible only if the semi-continuous model is adopted, this artifact becomes undetetectable and the calculated image is undistinguishable from the one calculated by the continuous anisotropic model [24], as shown in Fig. 6. This example clearly shows the usefulness of the new approach.

Let us briefly recall some of the experimental results reported in the paper by Tonomura *et al.* [30], whose main purpose was to investigate the formation mechanism of unconventional arrangements of vortices in high-

T_c superconducting thin films with an inclined applied magnetic field with respect to the layer plane. Out-of-focus observations were carried in the newly developed 1 MV electron microscope equipped with a special magnetic stage able to provide applied fields up to 10 mT along an arbitrary direction.

Film samples 300-400 nm thick of single-crystalline YBCO (T_c=92 K) were prepared by thinning a 30 μm×100 μm region with a focused ion beam machine (Hitachi FB-2000). These samples, whose surfaces were parallel to the ab-plane, were tilted around the y-axis of 30° whereas the electron beam was incident along the optical axis z. A magnetic field up to 10 mT was applied obliquely to the surface of the samples at incidence angles θ_H of 70°-90°, and vortices in arrangements reflecting the anisotropic layered structure of the materials were observed as Lorentz micrographs. The experimental results, taken with a defocus of 30 cm and at a temperature of 30 K are shown in Fig. 7, reproduced at large magnification so that contrast features of each single vortices are better visualized. The angle between the magnetic field and the surface normal varied between $\theta_H = 75°$ and $\theta_H = 85°$.

We note that each vortex has a circular shape for $\theta_H \leq 75°$, as shown in Fig. 7(a), and gradually elongates in the direction of the field when the angle is above 80°, as shown in Fig. 7(b), where the field was applied at $\theta_H = 82°$. At slightly higher angles, the shape changes dramatically, becoming dumbbell-like (Fig. 7(c), $\theta_H = 83°$) and even somewhat splitted in some cases, as emphasized by white arrows in Fig. 7(d), where $\theta_H = 84°$. For the largest angle, $\theta_H = 85°$, the vortices appear very elongated, with low contrast. At least one of them, indicated by an arrow in (e), shows a clear contrast splitting. These results can be interpreted by considering a core aligned with the field in the interior of the specimen, at an angle of 85°, and kinked near the surfaces and aligned perpendicularly to them. As remarked before, this fluxon core structure can be analysed only within the realm of the semicontinuous model. The results are shown in Figure 8 and are in good agreement with the experimental results, Fig. 7.

5 Parallel array of abrupt p-n junctions in a half-plane

Stimulated by the results obtained by the Fourier approach reported in the foregoing sections we endeavoured to apply this approach also to other long-

range electromagnetic fields. In fact, even if the solution of the problem is known by real space methods, the Fourier approach can offer a useful different perspective or, at least, a decrease computing times. This is the case of a parallel array of abrupt p-n junctions in a half-plane, tilted with respect to the specimen edge, for which an analytical model for the potential in the real space has been developed [35, 36]. As the specimen thickness has been neglected,the problem is equivalent to that of finding the electrostatic potential $V(x, y, z)$ produced by a parallel array of stripes having width b (and pitch in the y direction $b/\cos\alpha$) which lie in the positive half-plane ($z = 0; x \geq 0$), tilted at an angle α with respect to the edge normal ($-\pi/2 < \alpha < \pi/2$). The stripes are biased at alternate potential, namely $-V_R/2$ for p-doped and $V_R/2$ for n-doped stripes, so that this model corresponds to an array of abrupt step junctions. The model can be easily generalized to more realistic potentials by computing the appropriate coefficients for the Fourier series.

In Ref. [37, 38], this problem has been recasted in Fourier space. Writing the potential in the whole space as a Fourier series

$$V(x, y, z) = \sum_{n=-\infty}^{+\infty} \gamma_n V_n(x, z) e^{iyp_n} \tag{11}$$

with $p_n = (\pi n/b)\cos\alpha$ and where γ_n are the coefficient of the one-dimensional potential profile across two stripes of the array, we have shown that the 1D Fourier transform of $V_n(x, 0)$ is given by

$$\tilde{V}_n(k_x, 0) = \pi\delta(k_x - q_n) - \frac{i}{k_x - q_n}\frac{\sqrt{|p_n| - iq_n}}{\sqrt{|p_n| - ik_x}} \tag{12}$$

where $q_n = (\pi n/b)\sin\alpha$. The time-consuming integration of the potential in the real space for obtaining the phase shift associated, e.g., to the external field above the sample φ^I, in Fourier space becomes the multiplication of the 2D FT of the electrostatic potential in the $z = 0$ plane by the factor $C_E/\sqrt{k_x^2 + k_y^2}$. Explicitly, we have

$$\tilde{V}(k_x, k_y, 0) = 2\pi \sum_{n=-\infty}^{\infty} \gamma_n \delta(k_y - p_n)\tilde{V}_n(k_x, 0) \tag{13}$$

hence

$$\tilde{\varphi}^I(k_x, k_y) = 2\pi C_E \sum_{n=-\infty}^{\infty} \gamma_n \delta(k_y - p_n)\frac{\tilde{V}_n(k_x, 0)}{\sqrt{k_x^2 + k_y^2}} \tag{14}$$

Therefore, the external upper phase in real space can be written as a simple Fourier series

$$\varphi^I(x,y) = C_E \sum_{n=-\infty}^{\infty} \gamma_n \varphi_n(x) e^{ip_n y} \tag{15}$$

where the series coefficients are given by

$$\varphi_n(x) = \frac{1}{2\pi} \int dk_x \frac{\tilde{V}_n(k_x,0)}{\sqrt{k_x^2 + p_n^2}} e^{ixk_x} \tag{16}$$

Equation (16) can be evaluated by contour integration in the complex plane, yielding an explicit analytical expression for the phase coefficients in real space for the regions $x > 0$ (the junction array) and $x < 0$ (the vacuum)

$$\varphi_n(x<0) = \frac{1}{\sqrt{2|p_n|}} \frac{e^{x|p_n|}}{\sqrt{|p_n| - iq_n}} \tag{17}$$

$$\varphi_n(x>0) = \frac{e^{ixq_n}}{\sqrt{p_n^2+q_n^2}} \left[1 - \mathrm{Erfc}\sqrt{x(|p_n| + iq_n)}\right] + \frac{1}{\sqrt{2|p_n|}} \frac{e^{x|p_n|}}{\sqrt{|p_n| - iq_n}} \mathrm{Erfc}\sqrt{2x|p_n|} \tag{18}$$

where Erfc is the complementary error function. These results show that the phase shift of each Fourier component can be written in analytical form, so that the Gibbs phenomenon present in the former mixed numerical-analytical approach [37] is eliminated [38], as confirmed by Fig. 9(a) reporting the calculation of the total phase shift due to the external field above and below the sample.

Figure 9(b) reports also the result of the numerical calculation of the phase shift related to the boundary condition obtained by putting equal to zero the potential in the region $x < 0$ (i.e. in the vacuum) in the specimen-plane $z = 0$ [38]. This is the simplest and most natural choice when the exact solution of the electrostatic potential in the $z = 0$ plane is not known. Moreover, if we consider the analogy between electrostatic and optical problem, this choice reflects the one chosen by Kirchhoff in the analysis of diffraction problems, which is working well but has several fundamental limitations (see, e.g., the discussion in the Born and Wolf [39] or Goodman [40] books). The strong differences between images emphasize that in the electrostatic case

the phase is very sensitive to the boundary conditions: setting the potential beyond the edge of the specimen equal to zero is physically equivalent to a conducting region on the edge where screening charges are free to move and rearrange, thus modifying the field topography.

6 Stripe magnetic domains in a half-plane

Following the same formalism employed in developing the p-n junction models, we can extend phase computation through Fourier space to magnetic domains. The basic difference between electrostatics and magnetostatics, is that the latter involves a vector, rather than a scalar, potential. In addition, the absence of free charges in magnetism has the positive consequence that specifying a fixed and given distribution of sources (the arrangement of magnetic moments, or spins, in the material) is often more realistic and physically tenable than specifying fixed electric charge distributions, which is only reasonable for ideal insulators with no charge carrier mobility. Once the distribution or moments, i.e. the magnetization of the material or structure, is assigned, then the general expression linking magnetization and vector potential

$$\mathbf{A}(\mathbf{r}) = \frac{\mu_0}{4\pi} \int \mathbf{M}(\mathbf{r}') \times \frac{\mathbf{r} - \mathbf{r}'}{|\mathbf{r} - \mathbf{r}'|^3} d^3\mathbf{r}' \tag{19}$$

which can be found in any electromagnetism book (see, e.g., [41, 42]) represents the starting point of our calculations. The associated phase shift, according to equation (7.4) in chapter 7 of Ref. [7] **update and/or adjust this reference if necessary**, is then evaluated as a line integral along the electron trajectory, taken as the $z-$axis. Equation (19) can be written in Fourier Space, exploiting the convolution theorem and the linearity of the cross product, as

$$\tilde{\mathbf{A}} = \frac{\mu_0}{4\pi} \tilde{\mathbf{M}} \times \mathcal{F}\left[\frac{\mathbf{r}}{r^3}\right] \tag{20}$$

Therefore, by applying the formalism introduced in the previous sections, we can calculate the phase shift for interesting magnetostatic configurations. The 3D Fourier transform of the function $\mathbf{r}/r^3$, i.e. the kernel of eq. (19), can be calculated in cartesian coordinates by integrating with respect to each variable independently. The result turns out to be

$$\mathcal{F}\left[\frac{\mathbf{r}}{r^3}\right] = -4i\pi \frac{\mathbf{k}}{k^2} \tag{21}$$

Therefore, once the magnetization is given, the vector potential and the electron optical phase shift can be calculated in the Fourier space approach by means of

$$\tilde{\mathbf{A}}(\mathbf{k}) = -i\mu_0 \frac{\tilde{\mathbf{M}}(\mathbf{k}) \times \mathbf{k}}{k^2} \tag{22}$$

Let us now consider a thin specimen of thickness t, lying on the (x, y) plane and containing an array of 180° magnetic domains of width w each alternatively oriented along the positive or negative direction on the x-axis. The specimen is considered semi-infinite, which means that there is an abrupt termination along the y-axis at $x = 0$. The set-up is sketched in Fig. 10(a). Note that this is a truly three-dimensional problem, something that is extremely difficult to handle in electrostatics: the analogous problem of p-n junctions (one may imagine to substitute magnetic domains with equipotential regions in Fig. 10(a)) in a specimen of non-vanishing thickness is tremendously difficult to solve analytically, and escaped a solution so far.

The magnetization can be expressed as

$$\mathbf{M} = \frac{N\phi_\circ}{\mu_0 t w}[1, 0, 0] H(x) Q_w(y) U_t(z) \tag{23}$$

where N is the number of flux quanta trapped inside the domain (not necessarily an integer number, as the flux quantization does not apply here), $H(x)$ is the Heaviside step function, $Q_w(y)$ is a square wave of width w (period $2w$), and $U_t(z)$ is a hat function representing the thickness t. As the three functions in eq. (23) depend on different variables, we can express the Fourier transform of the magnetization as the product of the transforms of these functions, so that the Fourier transform of the $\mathbf{M}$ vector is

$$\tilde{\mathbf{M}} = \frac{N\phi_\circ}{\mu_0 w t}[1, 0, 0] \tilde{H}(k_x) \tilde{Q}_w(k_y) \tilde{U}_t(k_z) \tag{24}$$

Considering eq.(22), thus performing the cross product between the vectors $[1, 0, 0]$ and $\mathbf{k} = [k_x, k_y, k_z]$, and evaluating the FT of the three functions with the help of distribution theory, we can directly write the expression for the vector potential

$$\tilde{\mathbf{A}} = 8\pi \frac{N\phi_\circ}{w^2 t} \frac{[0, -k_z, k_y]}{k_y k_z k^2} \left[\pi\delta(k_x) + \frac{1}{ik_x}\right] \sum_n^{\text{odd}} \delta\left(k_y + \frac{\pi n}{w}\right) \sin\left(\frac{t k_z}{2}\right) \tag{25}$$

Extracting the z-component of the vector potential, performing the integration along the z-axis, going back to real space, we obtain the phase shift as a Fourier series

$$\varphi(x,y) = \frac{N}{2\pi}\mathrm{Re}\left(e^{i\pi y/w}\sum_{n=0}^{+\infty}\frac{e^{2ni\pi y/w}}{(n+1/2)^2}\left[2H(x) - \mathrm{S}(x)e^{-n\pi|x|/w}\right]\right) \tag{26}$$

Now, recalling the definition of the generalized Φ function (i.e. a generalization of the Riemann Zeta and Polylogarithmic functions), also called Lerch function [19], given by

$$\Phi_v^s(z) = \sum_{n=0}^{+\infty}\frac{z^n}{(n+v)^s} \tag{27}$$

where it is assumed that any term with $n+v=0$ is excluded, and considering the values $s=2$, $v=1/2$, we can sum the Fourier-Series, and obtain the final result in analytical form as

$$\varphi(x,y) = \frac{N}{2\pi}\mathrm{Re}\left[2H(x)e^{\pi\frac{iy}{w}}\Phi_{1/2}^2\left(e^{2\pi\frac{iy}{w}}\right) - \mathrm{S}(x)e^{\pi\frac{iy-|x|}{w}}\Phi_{1/2}^2\left(e^{2\pi\frac{iy-|x|}{w}}\right)\right] \tag{28}$$

The phase shift corresponding to a region enclosing three domains each carrying a single flux quantum is shown in Fig. 10(b) as a 4× amplified cosine map. The simulated holographic fringes are curved near the specimen edge indicating a strong demagnetizing effect. Moreover, inside the specimen (for $x > 0$) the fringes form a sharp angle over the domain wall, while in the vacuum they connect more smoothly. This effect is mainly due to the zero-width model assumed for the domain walls. An experimental example of stripe domain near the sample edge is shown in Fig. 10(c). The reconstructed phase shift associated to a stripe-magnetized region of a NdFeB sample is displayed as cosine map. Note the similarity between the simulated and experimental images, which, however, start to differ far from the edge because the sample thickness increases (a typical consequence of ion-milling). More realistic simulations with non-zero domain wall width can be performed by changing the square wave function $Q_w(y)$, and its Fourier transform, into a profile more representative of the magnetization topography across the wall. Clearly, in this case, the analytical expression (28) is no longer valid, but the phase shift can still be expressed as a Fourier series with suitable known coefficients.

7 Magnetic nanoparticles

As a further development of the Fourier space approach, we now turn our attention to magnetic nanoparticles. The computation of phase shifts associated to magnetized nanoparticles via Fourier space may be conveniently performed by introducing the characteristic function $D(\mathbf{r})$ associated to the particle shape, i.e. a function equal to one inside the particle and equal to zero outside. Whenever it is possible to perform the FT of $D(\mathbf{r})$, called $D(\mathbf{k})$ or shape amplitude, the corresponding phase shift can be derived analytically in Fourier space. In fact, the phase shift in Fourier representation turns out to be proportional to the value of the shape amplitude over a plane perpendicular to the reciprocal z-axis k_z. Let us briefly recall the procedure.

In general, we can write the magnetization vector associated to a uniformly magnetized nanoparticle as $\mathbf{M}(\mathbf{r}) = M_0\hat{\mathbf{m}}D(\mathbf{r})$, where M_0 is the saturation magnetization, and $\hat{\mathbf{m}}$ is the unit vector representing the magnetization direction and orientation. Hence, the Fourier representation of the magnetization is $\tilde{\mathbf{M}}(\mathbf{k}) = M_0\hat{\mathbf{m}}D(\mathbf{k})$. From equations (19) and (22) we can calculate directly the vector potential in Fourier space

$$\tilde{\mathbf{A}}(\mathbf{k}) = -iB_0D(\mathbf{k})\frac{\hat{\mathbf{m}}\times\mathbf{k}}{k^2} \tag{29}$$

where $\mu_0M_0 = B_0$ is the saturation magnetization expressed in Tesla.

From the knowledge of $\mathbf{A}$, one can easily calculate the magnetic induction, as $\mathbf{B}(\mathbf{r}) = \nabla\times\mathbf{A}(\mathbf{r})$, which in Fourier representation reads $\tilde{\mathbf{B}}(\mathbf{k}) = i\mathbf{k}\times\tilde{\mathbf{A}}(\mathbf{k})$, and the phase shift as a line-integral along the electron trajectory. The magnetic induction is computable as

$$\tilde{\mathbf{B}}(\mathbf{k}) = i\mathbf{k}\times\tilde{\mathbf{A}}(\mathbf{k}) = B_0D(\mathbf{k})\frac{\mathbf{k}\times\hat{\mathbf{m}}\times\mathbf{k}}{k^2} \tag{30}$$

which, exploiting the vector identity $\mathbf{k}\times\hat{\mathbf{m}}\times\mathbf{k} = \hat{\mathbf{m}}k^2 - \mathbf{k}(\mathbf{k}\cdot\hat{\mathbf{m}})$, can be also written, after an inverse Fourier transform, as the sum of the induction proportional to the magnetization and the demagnetization field:

$$\mathbf{B} = \mu_0\mathbf{M} - \frac{B_0}{8\pi^3}\int d^3\mathbf{k}\frac{D(\mathbf{k})}{k^2}\mathbf{k}(\hat{\mathbf{m}}\cdot\mathbf{k})e^{\mathbf{i}\mathbf{k}\cdot\mathbf{r}}. \tag{31}$$

The identification, based on the standard relation $\mathbf{B} = \mu_0(\mathbf{M}+\mathbf{H})$ linking the three fundamental magnetic fields, of the second term in equation

(31) as the demagnetization field generated by a uniformly magnetized particle of arbitrary shape led to an extensive treatment of demagnetization and shape effects in micromagnetism, ranging from the analytical solution for the point-function demagnetization tensor for faceted particles, to the exact computation of the demagnetization factors for important shapes such as disks, elliptic cylinders, rings, etc., to the development of a compact expression for the interaction energy between arbitrarily shaped magnetized shapes. Details of these advances are beyond the scope of this chapter, and the reader may refer to Refs.[43, 44, 45, 46, 47, 48, 49, 50, 51, 52]

The electrostatic phase φ_e, in absence of external charge distributions or applied electric fields, is simply proportional to the projected thickness of the particle t_p

$$\varphi_e = \frac{\pi V_0}{\lambda E} t_p, \tag{32}$$

where V_0 is the effective mean inner potential, i.e. the difference between the mean inner potential of the material and of the medium in which the particle is embedded (the vacuum is considered a medium with vanishing mean inner potential).

The magnetic phase φ_m, as usual, can be calculated from the knowledge of the vector potential. After integration along the z-axis, which is performed in Fourier space, we obtain

$$\tilde{\varphi}_m(\mathbf{k}) = \frac{\mathrm{i}\pi B_0}{\phi_0} \frac{D(k_x, k_y, 0)}{k_\perp^2} \left(\hat{\mathbf{m}} \times \mathbf{k}\right)\big|_z , \tag{33}$$

where $k_\perp = \sqrt{k_x^2 + k_y^2}$. Equation (33) suggests that, in order to calculate the phase shift of a uniformly magnetized nanoparticle, all we need to know is the shape amplitude, along with the direction and intensity of the magnetization. Note that equation (33) can be interpreted as a manifestation of the Fourier projection-slice theorem (see e.g. [53]).

7.1 Basic shapes and faceted magnetic nanoparticles

With the availability of equation (33), we only need to provide the shape amplitude in order to calculate the phase shift in Fourier space. We list a collection of shape amplitudes for the most basic shapes (prism, cylinder, ellipsoid, sphere), for less common but important shapes (ring and elliptic cylinder), and for faceted particles. For each of the shapes considered,

sketched in Fig.11(a-c,g-i), we also write explicitely the Fourier representation of the phase shift. For all shapes, the magnetization ($M_0 = B_0/\mu_0$ is the particle saturation magnetization) is assumed uniform along the x-axis without loss of generality.

7.1.1 Prism

A rectangular prism (P) of sides $(2L_x, 2L_y, 2L_z)$, Fig.11(a):

$$D^{\mathrm{P}}(\mathbf{k}) = V_{\mathrm{P}}\mathrm{sinc}(L_x k_x)\mathrm{sinc}(L_y k_y)\mathrm{sinc}(L_z k_z), \tag{34}$$

where $V_{\mathrm{P}} = 8L_xL_yL_z$ is the prism volume, and $\mathrm{sinc}(x) = \sin(x)/x$;

$$\tilde{\varphi}_m^{\mathrm{P}}(\mathbf{k}) = \frac{\mathrm{i}\pi B_0 V_{\mathrm{P}}}{\phi_0}\frac{k_y}{k_\perp^2}\mathrm{sinc}(L_x k_x)\mathrm{sinc}(L_y k_y), \tag{35}$$

7.1.2 Ellipsoid and sphere

An ellipsoid (E) of semi-axes (a, b, c), Fig.11(c):

$$D^{\mathrm{E}}(\mathbf{k}) = 3V_{\mathrm{E}}\frac{j_1(q)}{q} \tag{36}$$

where $j_1(q)$ is a spherical Bessel function and $q^2 = a^2k_x^2 + b^2k_y^2 + c^2k_z^2$. Note that $\lim_{q\to 0} j_1(q)/q = 1/3$, so that $D^{\mathrm{E}}(0) = (4/3)\pi abc = V_{\mathrm{E}}$, which is the volume of the ellipsoid, as it should be. When $a = b = c = R$, the expression reduces to the shape amplitude for a sphere (S), Fig.11(b):

$$D^{\mathrm{S}}(\mathbf{k}) = 4\pi R^2\frac{j_1(kR)}{k} \tag{37}$$

The phase shifts are:

$$\tilde{\varphi}_m^{\mathrm{E}}(\mathbf{k}) = \frac{3\mathrm{i}\pi B_0 V_{\mathrm{E}}}{\phi_0}\frac{k_y}{k_\perp^2}\frac{j_1(q')}{q'} \tag{38}$$

with $q' = \sqrt{a^2k_x^2 + b^2k_y^2}$, and

$$\tilde{\varphi}_m^{\mathrm{S}}(\mathbf{k}) = \frac{3\mathrm{i}\pi B_0 V_{\mathrm{E}}}{\phi_0}\frac{k_y}{k_\perp^2}\frac{j_1(k_\perp R)}{k_\perp R} \tag{39}$$

7.1.3 Cylinder

A cylindrical (C) particle of radius R and thickness $t = 2d$, Fig.11(g):

$$D^{\mathrm{C}}(\mathbf{k}) = \frac{2\pi Rt}{k_\perp} J_1(k_\perp R)\mathrm{sinc}(dk_z), \tag{40}$$

where $J_1(x)$ is the Bessel function of first order and $V_C = \pi R^2 t$ is the particle volume; the phase shift is:

$$\tilde{\varphi}_m^{\mathrm{C}}(\mathbf{k}) = \frac{2\mathrm{i}\pi B_0 V_{\mathrm{C}}}{\phi_0} \frac{k_y}{k_\perp^2} \frac{J_1(k_\perp R)}{k_\perp R}. \tag{41}$$

7.1.4 Elliptic cylinder

An elliptic-cylindrical (EC) particle of semi-axes (a, b), and thickness $t = 2d$, Fig.11(h):

$$D^{\mathrm{EC}}(\mathbf{k}) = 2V_{EC} \frac{J_1(q)}{q} \mathrm{sinc}(dk_z), \tag{42}$$

where now $q^2 = a^2 k_x^2 + b^2 k_y^2$ and the particle volume is $V_{EC} = \pi abt$. Note that when $a = b = R$ the shape amplitude reduces to the cylindrical case.

$$\tilde{\varphi}_m^{\mathrm{EC}}(\mathbf{k}) = \frac{2\mathrm{i}\pi B_0 V_{\mathrm{EC}}}{\phi_0} \frac{k_y}{k_\perp^2} \frac{J_1(q)}{q} \tag{43}$$

7.1.5 Ring with rectangular cross section

A ring (R) particle of inner radius R_1, outer radius R_2, and thickness $t = 2d$, Fig.11(i):

$$D^{\mathrm{R}}(\mathbf{k}) = \frac{2\pi t}{k_\perp} \left[R_2 J_1(k_\perp R_2) - R_1 J_1(k_\perp R_1)\right] \mathrm{sinc}(dk_z), \tag{44}$$

where

$$\tilde{\varphi}_m^{\mathrm{R}}(\mathbf{k}) = \frac{2\mathrm{i}\pi^2 B_0 t}{\phi_0} \frac{k_y}{k_\perp^3} \left[R_2 J_1(k_\perp R_2) - R_1 J_1(k_\perp R_1)\right] \tag{45}$$

The phase shift associated to each of these basic shapes is shown in Fig.11(d-f,j-l) as a cosine map. Each of the shapes carries a single flux quantum, i.e. $B_0 S = \phi_0$, where S is the appropriate cross section perpendicular to the magnetization direction ($S = 4L_y L_z$ for the prism, $S = \pi R^2$ for the sphere, $S = 2Rt$ for the cylinder, etc.). By imposing this condition of flux

equality between shapes, one can observe the different degree of demagnetization: the number of fringes is different for each shape, indicating a different intensity of the demagnetization field which effectively decreases the magnetic induction, and hence the strength of the dipole field at large distances, associated to each nanoparticle. Note also the flat phase in the inner region of the ring, Fig.11(l), indicating a degree of magnetic shielding as the induction lines flow preferentially in the permeable ferromagnetic part of the element.

7.1.6 Faceted particles

The shape amplitude of a faceted particle (F) with E edges and F faces is given by [54]:

$$D^{\mathrm{F}}(\mathbf{k}) = -\frac{1}{k^2}\sum_{f=1}^{F}\frac{\mathbf{k}\cdot\mathbf{n}_f}{k^2-(\mathbf{k}\cdot\mathbf{n}_f)^2}\sum_{e=1}^{E_f}L_{fe}\mathbf{k}\cdot\mathbf{n}_{fe}\mathrm{sinc}(\frac{L_{fe}}{2}\mathbf{k}\cdot\mathbf{t}_{fe})e^{-\mathrm{i}\mathbf{k}\cdot\xi^C_{fe}}. \quad (46)$$

This equation is only valid if the second denominator is non-zero. If $\mathbf{k} = \pm k\mathbf{n}_f$ (in other words, if $\mathbf{k}$ is parallel to any one of the face normals), then the contribution of that particular face (or faces) must be replaced by

$$D^{\mathrm{F}}_f(\mathbf{k}) = \mathrm{i}\frac{\mathbf{k}\cdot\mathbf{n}_f}{k^2}P_f e^{-\mathrm{i}d_f\mathbf{k}\cdot\mathbf{n}_f}, \quad (47)$$

where P_f is the surface area of the face f, and d_f the distance between the origin and the face f. In the origin of Fourier space, the shape amplitude is equal to the particle volume, i.e. $D(\mathbf{0}) = V$. The symbols in equation (46) are defined as (see also figure 12):

- ξ^C_{fe}: coordinate vectors of the center of the edge e of face f;
- $\mathbf{n}_f$: unit outward normal to face f;
- L_{fe}: length of the e-th edge of the f-th face;
- $\mathbf{t}_{fe}$: unit vector along the e-th edge of the f-th face, defined by

  $$\mathbf{t}_{fe} = \frac{\mathbf{n}_f \times \mathbf{N}_{fe}}{|\mathbf{n}_f \times \mathbf{N}_{fe}|},$$

  where $\mathbf{N}_{fe}$ is the unit outward normal *on* the face which has the edge e in common with the face f;

- $\mathbf{n}_{fe}$: unit outward normal *in* the face f on the edge e defined by $\mathbf{n}_{fe} = \mathbf{t}_{fe} \times \mathbf{n}_f$.

The input parameters needed to complete this computation for an arbitrary polyhedron are the N_v vertex coordinates ξ_v and a list of which vertices make up each face (counterclockwise when looking towards the polyhedron center). All other quantities can be computed from these parameters.

The phase shift can be calculated by inserting $D(k_x, k_y, 0)$, i.e. the limit $k_z \to 0$ of the shape amplitude (46), into equation (33). Its expression, however, requires the help of a computer algebra software such as Mathematica [55] in order to be evaluated explicitely. In fact, only in a few simple cases the explicit analytical expression for the phase shift is compact enough to be written conveniently. Two examples which are simple enough to be evaluated explicitely are the triangular platelet, and the sheared rectangle, both described in [57], and both important building blocks for constructing more complex regular or irregular polygonal shapes. Having simple building blocks available is important to simulate phase shift associated for instance to the triangular closure-domains often observed at the edges of a sample, or, more in general, magnetization topographies which differ substantially from the simple uniform case within a basic shape.

Figure 13 shows the magnetic and electrostatic phase shifts for all Platonic and Archimedian shapes. For each polyhedron, a pair of grayscale images is shown. The image on the left corresponds to the difference between the magnetic phase shift for the uniformly magnetized polyhedron and the magnetic phase shift for the uniformly magnetized sphere with the same volume. The volume was taken to be 10^6 nm^3 for all particles, so that the edge length corresponds to the values shown in table 1. All magnetic phase shift differences are shown on a common intensity scale. The phase shift for a polyhedral particle may locally be up to about 15% different from that for a sphere of the same volume. In the vacuum area surrounding each particle, the phase shift is almost identical to that for the sphere. This is due to the fact that at a large distance the fringing field for all particles approaches that of a magnetic dipole. The phase difference images in figure 13 indicate that in order to determine the magnetic component of the phase shift, both a high spatial resolution and a high phase resolution are required. Furthermore, the electrostatic phase shift adds to the magnetic phase shift, complicating further the determination of the magnetization state of the particle. The electrostatic phase shift is shown as a grayscale plot on the right hand side

of each pair of images in figure 13. Superimposed on the projected thickness is a projection of the polyhedron in the orientation used for the computation. The fine structure of both magnetic and electrostatic phases depends sensitively on the precise orientation of the polyhedron.

7.2 Electrostatic versus magnetic phase-shifts

It is of importance to compare the electrostatic and magnetic contributions to the phase shift in a circularly magnetized spherical particle, as this can give useful hints on the capabilities of TEM to retrieve a magnetic signal from nanoparticles. The electrostatic and magnetic contributions to the phase shift strongly depend on the particle radius. If we choose a favorable condition for the observation, i.e. a reasonably high accelerating voltage (300 kV), and an embedding medium with a mean inner potential not very different from that of the magnetic particle (e.g. $\Delta V = 10$ V), we can plot φ as a function of the particle radius R (figure 14(a)). We can define the characteristic radius $R_c = 4\phi_0 \Delta V / \pi \lambda E B_0 = 34$ nm, for which electrostatic and magnetic contributions are equal. For smaller R, the electrostatic contribution is predominant, and overwhelms the magnetic phase, which reaches the limit of detectability (here assumed equal to $\pi/20$) around the $R = 7$ nm, as displayed in figure 14b.

For a spherical particle of radius $R = R_c/2 = 17$ nm the magnetic signal can be considered as a perturbation with respect to the predominant electrostatic phase shift shown in (e). This poses a serious limitation in the TEM usefulness for magnetic observations. However, with a careful choice of the experimental set-up and specimen geometry, it is possible to reach the now inaccessible region under R_c.

The assumed limit of detectability $\pi/20$ is actually very dependent on the experimental set-up, and on the phase retrieval technique employed. As electron holography is generally claimed to be a technique capable of retrieving the phase shifts as small as $\pi/100$ [25], in principle there is no lower limit for extracting the magnetic signal for nanoparticles with TEM, as $\pi/100$ corresponds to a particle radius smaller than 3 nm, which is very close to the atomic scale. Certainly, the electrostatic contribution should be precisely taken into account first, otherwise the real limit for magnetic observation in TEM remains R_c. A thorough analysis of the problems involved in the separation of the magnetic and electrostatic components by in-situ magnetization reversal was given by [58].

8 Conclusions

It has been shown in this work that the Fourier space approach can be fruitfully applied to the calculation of the fields and the associated electron optical phase shift of several magnetic and electrostatic structures, like superconducting vortices in conventional and high-T_c superconductors, reverse biased p-n junctions, magnetic domains and nanoparticles. In all these cases, this novel approach has led to unexpected but extremely interesting results, very often expressed in analytical form, which allow the quantitative and reliable interpretation of the experimental data collected by means of electron holography or of more conventional Lorentz microscopy techniques. Moreover, it is worth recalling that whenever long-range electromagnetic fields are involved, a physical model of the object under investigation is necessary in order to take into account correctly the perturbation of the reference wave induced by the tail of the field protruding into the vacuum. For these reasons, we believe that the Fourier space approach for phase computations we have introduced and discussed in this chapter will represent an invaluable tool for the investigation of electromagnetic fields at the meso- and nano-scale.

Acknowledgements

The authors are indebted to their many colleagues from Japan, cited as coauthors in the reference list, who contributed to the research on superconducting vortices. Part of the research on magnetic phase computations was carried out in collaboration with Prof. Marc De Graef, whose essential contribution is gratefully acknowledged. One of the authors (MB) would like to thank in particular Yimei Zhu and Marvin A. Schofield for useful discussions and contributions to the experiments on magnetic nanostructures. Financial support was partially provided by the U.S. Department of Energy, Basic Energy Sciences, Contract No. DE-AC02-98CH10886. Two of the authors (GP and MB) acknowledge a collaboration scheme with the Advanced Research Laboratory, Hitachi Ltd., Japan, which provided also partial financial support.

References

[1] T. Kawasaki, T. Yoshida, T. Matsuda, N. Okasabe, A. Tonomura, I. Matsui and K. Kitazawa, Appl. Phys. Lett. **76**, 1342 (2000).

[2] T. Akashi, K. Harada, T. Matsuda, H. Kasai, A. Tonomura, T. Furutsu, N. Moriya, T. Yoshida, T. Kawasaki, K. Kitazawa and H. Koinuma, Appl. Phys. Lett. **81**, 1922 (2002).

[3] K. Harada, A. Tonomura, Y. Togawa, T. Akashi and T. Matsuda, Appl. Phys. Lett. **84**, 3229 (2004).

[4] K. Harada, A. Tonomura, T. Matsuda, T. Akashi and Y. Togawa, J. Appl. Phys. **96**, 6097 (2004).

[5] K. Harada, T. Akashi, Y. Togawa, T. Matsuda and A. Tonomura, Jap. J. Appl. Phys. **44**, L636 (2005).

[6] K. Harada, T. Akashi, Y. Togawa, T. Matsuda and A. Tonomura, J. Electron Microsc. **54**, 19 (2005).

[7] E. Völkl, L.F. Allard, D. Joy (Editors), Introduction to Electron Holography, Kluwer Academic/Plenum Publishers, New York, 1999.

[8] K. Harada, T. Matsuda, J.E. Bonevich, M. Igarashi, S. Kondo, G. Pozzi, U. Kawabe and A. Tonomura, Nature **360**, 51 (1992).

[9] J.E. Bonevich, K. Harada, T. Matsuda, H. Kasai, T. Yoshida, G. Pozzi and A. Tonomura, Phys. Rev. Lett. **70**, 2952 (1993).

[10] J.E. Bonevich, K. Harada, H. Kasai, T. Matsuda, T. Yoshida, G. Pozzi and A. Tonomura, Phys. Rev. B **49**, 6800 (1994).

[11] M. Beleggia, Phys. Rev. B **69**, 014518 (2004).

[12] T. Yoshida, J. Endo, H. Kasai, K. Harada, N. Osakabe, A. Tonomura and G. Pozzi, J. Appl. Phys. **85** (1999) 1228.

[13] T. Yoshida, J. Endo, K. Harada, H. Kasai, T. Matsuda, O. Kamimura, A. Tonomura, M. Beleggia, R. Patti and G. Pozzi, J. Appl. Phys. **85** (1999) 4096.

[14] A. Migliori, G. Pozzi and A. Tonomura, Ultramicroscopy **49**, 87 (1993).

[15] R.P. Huebener, Magnetic Flux Structures in Superconductors, Vol. 6 of Springer Series in Solid State Sciences, Springer, Berlin, 1979.

[16] J.E. Bonevich, D. Capacci, K. Harada, H. Kasai, T. Matsuda, R. Patti, G. Pozzi and A. Tonomura, Phys. Rev. B **57**, 1200 (1998).

[17] M. Beleggia and G. Pozzi, Ultramicroscopy 84 (2000) 171.

[18] M. Beleggia and G. Pozzi, Phys. Rev. B 63 (2001) 54507.

[19] I.S. Gradshtein and I.M. Ryzhik, Table of Integrals, Series and Products, Academic Press, San Diego, 1980.

[20] R.N. Bracewell, Two-Dimensional Imaging, Prentice Hall, Englewood Cliffs, New Jersey, 1995.

[21] R. Patti and G. Pozzi, Ultramicroscopy **77**, 163 (1999).

[22] A. Tonomura, H. Kasai, O. Kamimura, T. Matsuda, K. Harada, Y. Nakayama, J. Shimoyama, K. Kishio, T. Hanaguri, K. Kitazawa, M. Sasase and S. Okayasu, Nature **412**, 620 (2001).

[23] O. Kamimura, H. Kasai, T. Akashi, T. Matsuda, K. Harada, J. Masuko, T. Yoshida, N. Osakabe, A. Tonomura, M. Beleggia, G. Pozzi, J. Shimoyama, K. Kishio, T. Hanaguri, K. Kitazawa, M. Sasase and S. Okayasu, J. Phys. Soc. Japan **71**, 1840 (2002).

[24] M. Beleggia, G. Pozzi, J. Masuko, N. Osakabe, K. Harada, T. Yoshida, O. Kamimura, H. Kasai, T. Matsuda and A. Tonomura, Phys. Rev. B **66**, 174518 (2002).

[25] A. Tonomura, Electron Holography, Springer, Berlin (1993).

[26] G. Blatter, M.V. Feigel'man, V.B. Geshkenbein, A.I. Larkin and V.M. Vinokur, Rev. Mod. Phys. **66**, 1125 (1994).

[27] E.H. Brandt, Rep. Prog. Phys. **58**, 1465 (1995).

[28] J.R. Clem, Phys. Rev. B **43**, 7837 (1991).

[29] R.G. Mints, V.G. Kogan and J.R. Clem, Phys. Rev. B **61**, 1623 (2000).

[30] A. Tonomura, H. Kasai, O. Kamimura, T. Matsuda, K. Harada, T. Yoshida, T. Akashi, J. Shimoyama, K. Kishio, T. Hanaguri, K. Kitazawa, T. Masui, S. Tajima, N. Koshizuka, P.L. Gammel, D. Bishop, M. Sasase and S. Okayasu, Phys. Rev. Lett. **88**, 237001 (2002).

[31] J.R. Clem, Phys. Rev. B **43**, 7837 (1991).

[32] J.R. Clem, Physica C **235-240**, 2607 (1994).

[33] M.W. Coffey and E.T. Phipps, Phys. Rev. B **53**, 389 (1996).

[34] M. Beleggia, G. Pozzi, A. Tonomura, H. Kasai, T. Matsuda, K. Harada, T. Akashi, T. Masui, S. Tajima, Phys. Rev. B **70**, 184518 (2004).

[35] C. Capiluppi, A. Migliori and G. Pozzi, Microsc. Microanal. Microstruct. 6 (1995) 647.

[36] M. Beleggia, R. Capelli and G. Pozzi, Philos. Mag. B **80**, 1071 (2000).

[37] M. Beleggia, P.F. Fazzini and G. Pozzi, Ultramicroscopy **96**, 93 (2003).

[38] P.F. Fazzini, G. Pozzi and M. Beleggia, Ultramicroscopy **104**, 193 (2005).

[39] M. Born and E. Wolf, Principles of Optics, Cambridge University Press, 7th Ed., 1999.

[40] J.W. Goodman, Introduction to Fourier Optics, Roberts and Company Publishers, 3rd Ed., 2004.

[41] M. Mansuripur, The Physical Principles of Magneto-optical Recording, Cambridge University Press, 1995.

[42] J.D. Jackson, Classical Electrodynamics, Wiley, 3rd Ed., 1998.

[43] M. Beleggia and M. De Graef. J. Magn. Magn. Mater. 263, L1-L9 (2003).

[44] S. Tandon, M. Beleggia, Y. Zhu, M. De Graef. J. Magn. Magn. Mater. 271, 9-26 (2004).

[45] S. Tandon, M. Beleggia, Y. Zhu, M. De Graef. J. Magn. Magn. Mater. 271, 27-38 (2004).

[46] M. Beleggia and M. De Graef. J. Magn. Magn. Mater. 285, L1-L10 (2005).

[47] M. De Graef and M. Beleggia, J. Magn. Magn. Mater. 305/2, 403-409 (2006).

[48] M. Beleggia, J.W. Lau, M.A. Schofield, Y. Zhu, S. Tandon and M. De Graef. J. Magn. Magn. Mater. 301, 131-146 (2006).

[49] M. Beleggia, M. De Graef, Y.T. Millev, D.A. Goode and G. Rowlands. J. Phys. D: Appl. Phys. 38, 3333-3342 (2005).

[50] M. Beleggia, M. De Graef and Y.T. Millev. J. Phys. D: Appl. Phys. 39, 891-899 (2006).

[51] M. Beleggia, M. De Graef and Y.T. Millev. Philos. Mag. 86, 2451-2466 (2006).

[52] M. Beleggia, M.A. Schofield, Y. Zhu, M. Malac, Z. Liu, M. Freeman. Appl. Phys. Lett. 83, 1435-1437 (2003).

[53] R.N. Bracewell, Science 248, 697 (1990).

[54] J. Komrska, Optik, **80**, 171 (1987).

[55] S. Wolfram *Mathematica*, Version 4.0, Wolfram Research Inc., Champaign, IL, 1999.

[56] M. Beleggia and Y. Zhu. Philos. Mag. 83, 1045-1055 (2003).

[57] M. Beleggia, Y. Zhu, S. Tandon, M. De Graef. Philos. Mag. 83, 1143-1161 (2003).

[58] R.E. Dunin-Borkowski, M.R. McCartney, D.J. Smith, S. Parkin, Ultramicroscopy, **74**, 61 (1998).

Table 1: Number of vertices N_v, edges N_e, and facesN_f for the 5 Platonic and 13 Archimedian solids, along with the volume factor V_s. The total volume is given by $V = V_s L^3$, with L the edge length. The edge length L for a representative volume of 10^6 nm^3 is shown in the last column.

Polyhedron	N_v	N_e	N_f	V_s	L [nm]	Fig. 13
tetrahedron	4	6	4	0.118	204.0	a
cube	8	12	6	1.000	100.0	b
octahedron	6	12	8	0.471	128.5	c
dodecahedron	20	30	12	7.663	50.72	d
icosahedron	12	30	12	2.182	77.10	e
truncated octahedron	24	36	14	11.31	44.54	f
cuboctahedron	12	24	14	2.357	75.14	g
rhombitruncated cuboctahedron	48	72	26	41.80	28.81	h
snub cube	24	60	38	7.890	50.23	i
rhombicuboctahedron	24	48	26	8.714	48.59	j
truncated cube	24	36	14	13.60	41.89	k
truncated icosahedron	60	90	32	55.29	26.25	l
icosidodecahedron	30	60	32	13.84	41.65	m
rhombitruncated icosidodecahedron	120	180	62	206.8	16.91	n
snub dodecahedron	60	150	92	37.62	29.84	o
rhombicosidodecahedron	60	120	62	41.61	28.86	p
truncated dodecahedron	60	90	32	85.04	22.74	q
truncated tetrahedron	12	18	8	2.711	71.72	r

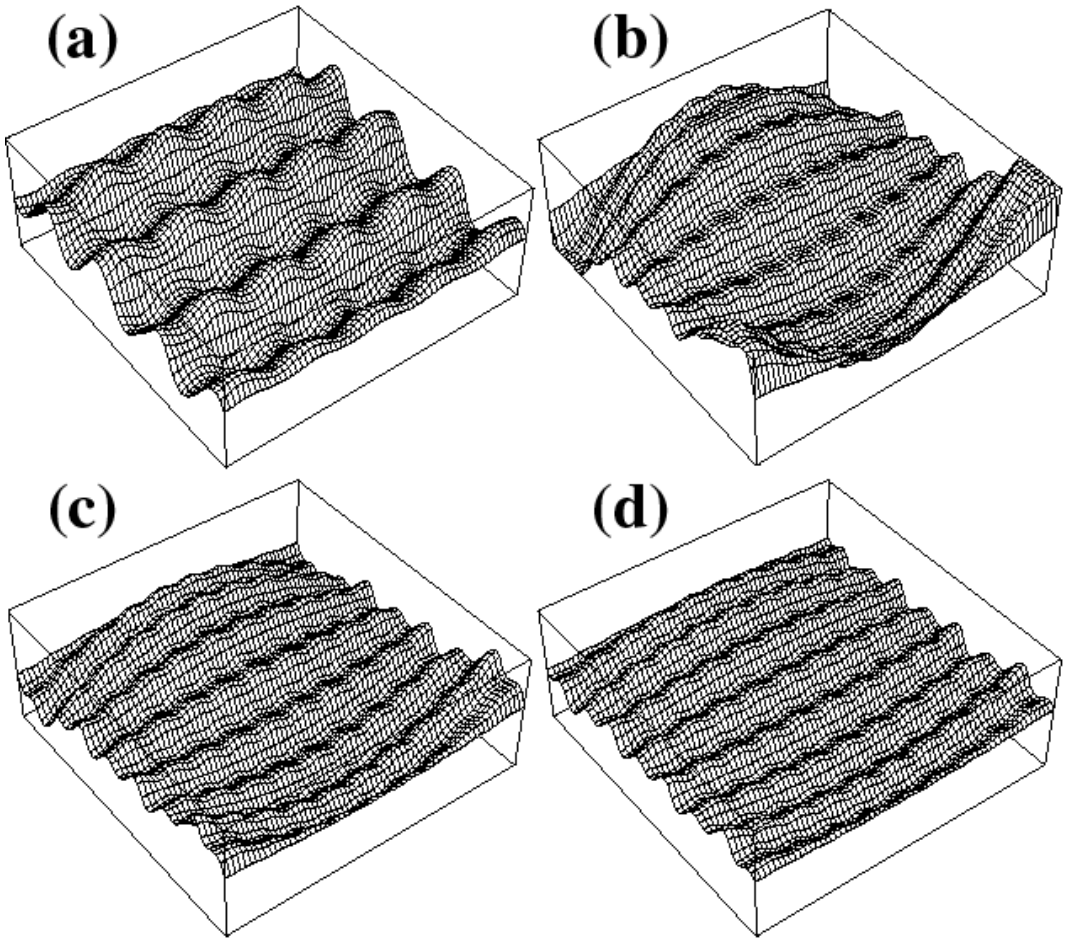

Figure 1: Vortex finite-lattice phase shift with variable spacing s and total number of vortices n_v: (a) s=300 nm, n_v=331; (b) s=150 nm, n_v=331; (b) s=150 nm, n_v=1261; (b) s=150 nm, n_v=4921. Only the central part of the finite-lattice, containing about 20 vortices, is displayed.

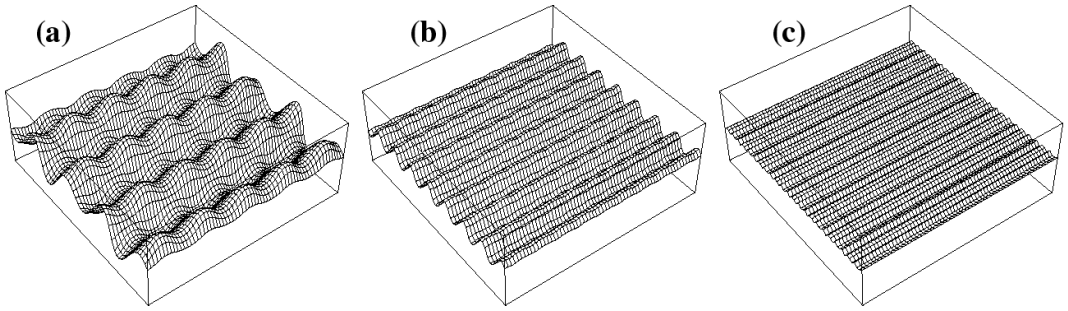

Figure 2: Vortex lattice Fourier-series phase shift with variable spacing s: (a) s=300 nm (to be compared with Fig. 1(a)); (b) s=150 nm (to be compared with Fig. 1(b)); (c) s=50 nm. The number of Fourier coefficient was suitably chosen depending on the lattice spacing.

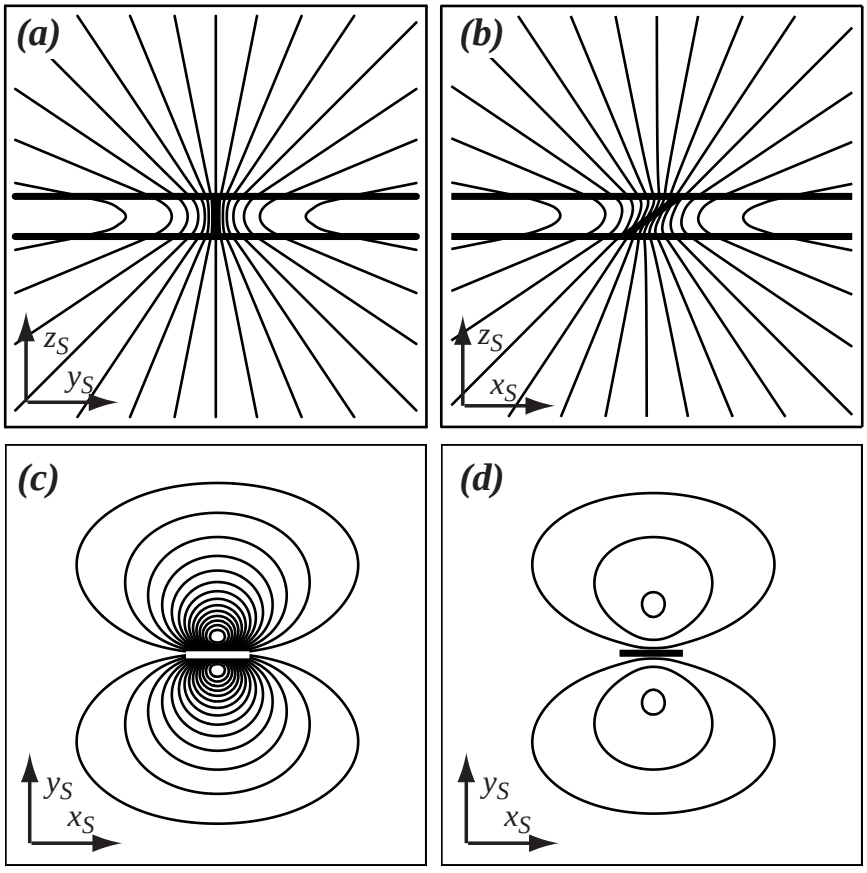

Figure 3: Figure 3: Contour line plots representing the phase shift in three orthogonal directions x_S (a), y_S (b) and z_S (c,d). (a,b,c) isotropic case $\gamma = 1$; (d) medium anisotropy case $\gamma = 5$. The contour lines represent phase shifts of 200 mrad in (a,b) and of 30 mrad in (c,d). Simulation parameters: tilt angle $\theta = 45^\circ$, $\lambda_{ab} = 200$ nm, plot region 4 μm.

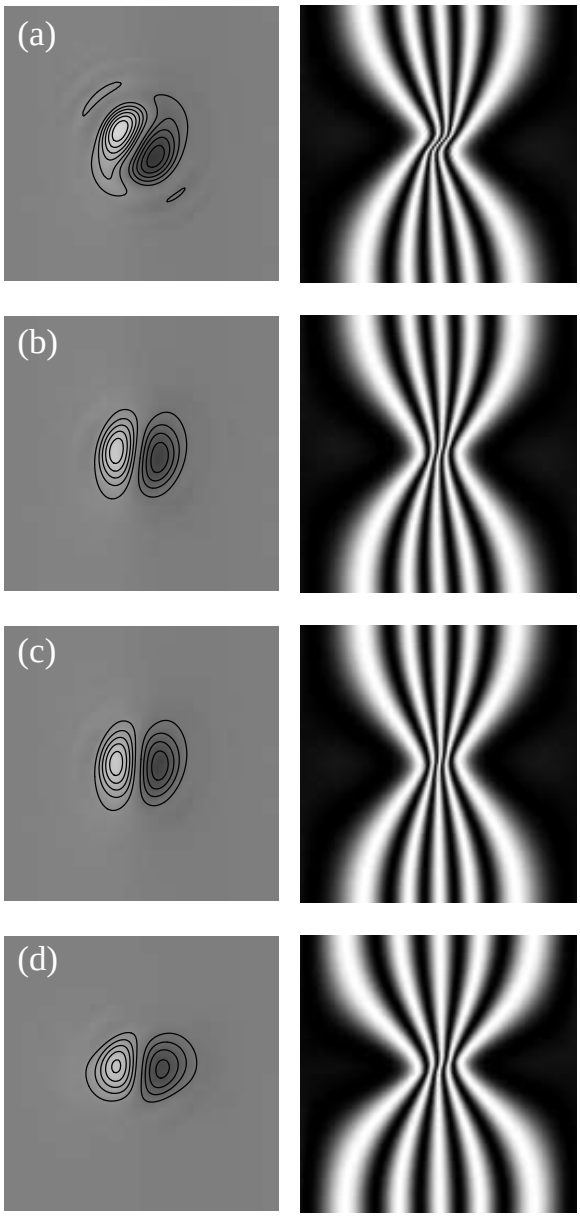

Figure 4: Out-of-focus images (left column) and holographic contour maps $32\times$ amplified (right column) for the following values of the anisotropic parameter: $\gamma = 1, 5, 50, \infty$ (from top to bottom). The columnar defect tilt angle is $\theta = 45^\circ$ and the specimen rotation is $\beta = 90^\circ$.

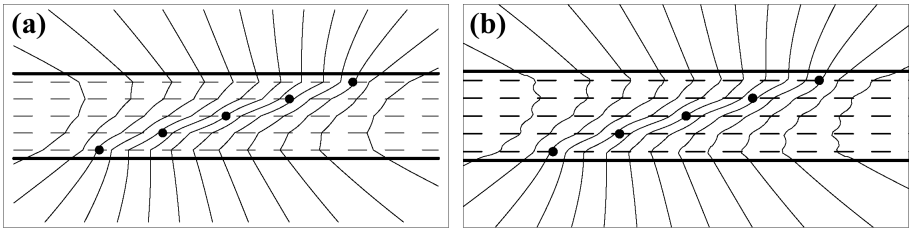

Figure 5: Contour line plots representing the phase shift along y_S calculated with the the pancake (a) and semicontinuous (b) models (n_L=5 layers). The phase lines represent shifts of 200 mrad. Simulation parameters: tilt angle of the stack of pancakes $\theta = 75°$, plot region 2×1 μm, specimen thickness t=400 nm and λ=200 nm. The dots marks the positions of the pancake vortices.

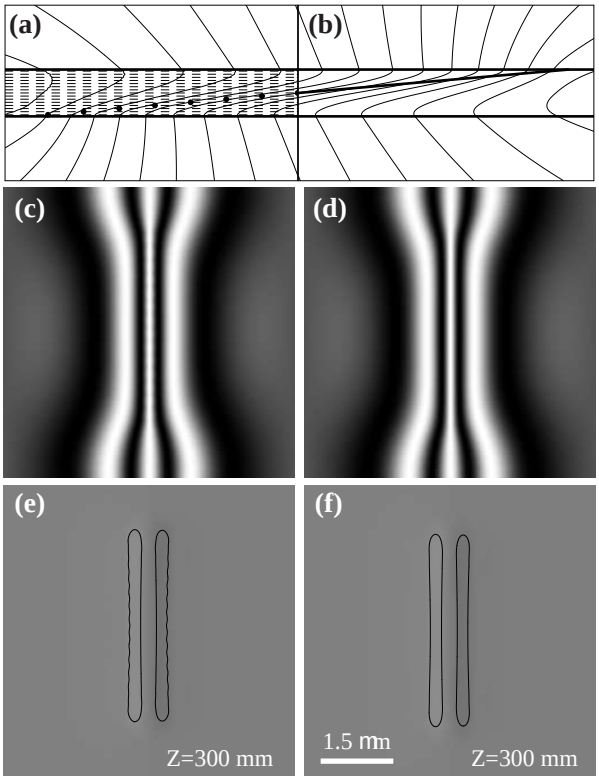

Figure 6: Comparison between the semi-continuous (left column) and the continuous-anisotropic (right column) models. (a,b) Phase contour line plot over a region of 5×1 μm; (c,d) holographic contour maps 32× amplified, (e,f) out-of-focus images (defocus value $Z = 300$ mm). Simulation parameters: pancake stack/vortex core tilt angle $\theta = 85°$, specimen tilt and rotation $\alpha = 30°$, $\beta = 0°$, number of layers $n_L = 15$, specimen thickness 400 nm, anisotropy factor $\gamma = 200$, λ=200 nm. Each contour line superimposed to the out-of-focus images represents a contrast variation of 3%.

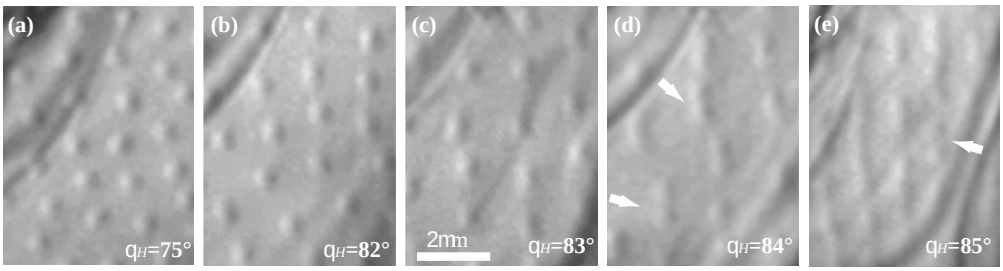

Figure 7: Lorentz micrographs of vortices in YBCO film sample at tilted magnetic fields (T=30 K, $|\mathbf{H}_{\rm app}|$=0.3 mT, angles indicated in the figure). When the tilt angle becomes larger than 80°, the vortex images start elongating (b,c). For the applied field angle of 84° we observe dumbbell features, and apparent splitting of the vortex contrast, as indicated by white arrows in (d). For the largest angle, 85°, vortices appear very elongated, with remaining indication of stack splitting.

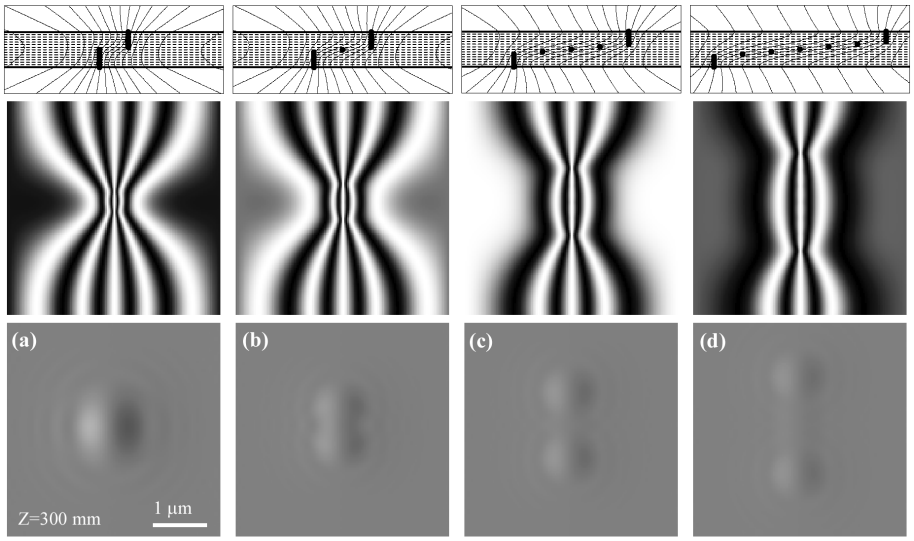

Figure 8: Simulation series for exotic (kinked) core structures, where the pancakes are distributed according to the dots in the phase contour line plots. From top to bottom: phase contour line plot over a region of 2.5×1 μm, where each contour line represents a phase variation of $\pi/16$; holographic cosine map, 32× amplified; out-of-focus images with Z=300 mm. Simulation parameters: specimen tilt and rotation $\alpha = 30°$, $\beta = 0°$, specimen thickness 400 nm, number of layers n_L=15, λ=200 nm.

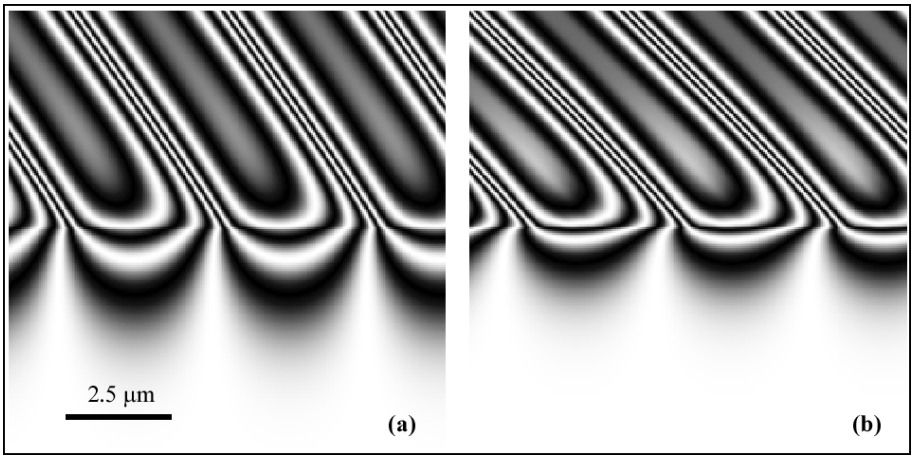

Figure 9: (a) analytical phase shift for a semi-infinite array of abrupt p-n junctions tilted at 45° with respect to the specimen edge and with an alternating bias of 1 V. (b) phase shift resulting from a non-physical choice of the electrostatic potential in the specimen plane. The phase shift is displayed as a 2× amplified cosine map.

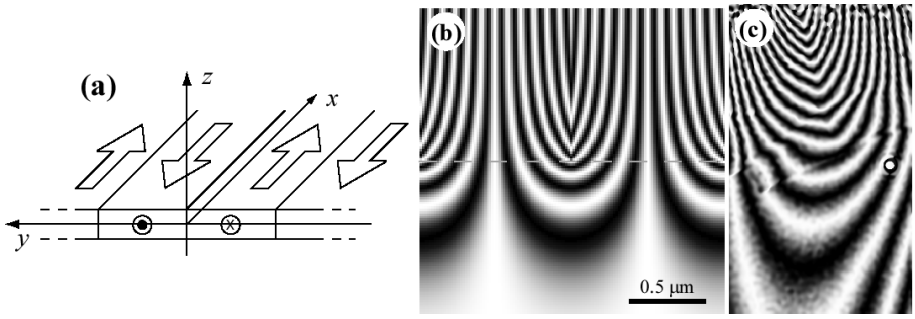

Figure 10: (a) magnetic stripe domains near the edge of a thin film; (b) phase shift, displayed as a 24× amplified cosine map, associated to stripe domains each carrying a single flux quantum (the grey dashed line in (b) indicates the sample edge); (c) experimental phase shift retrieved by electron holography over a region near the edge of a NdFeB sample.

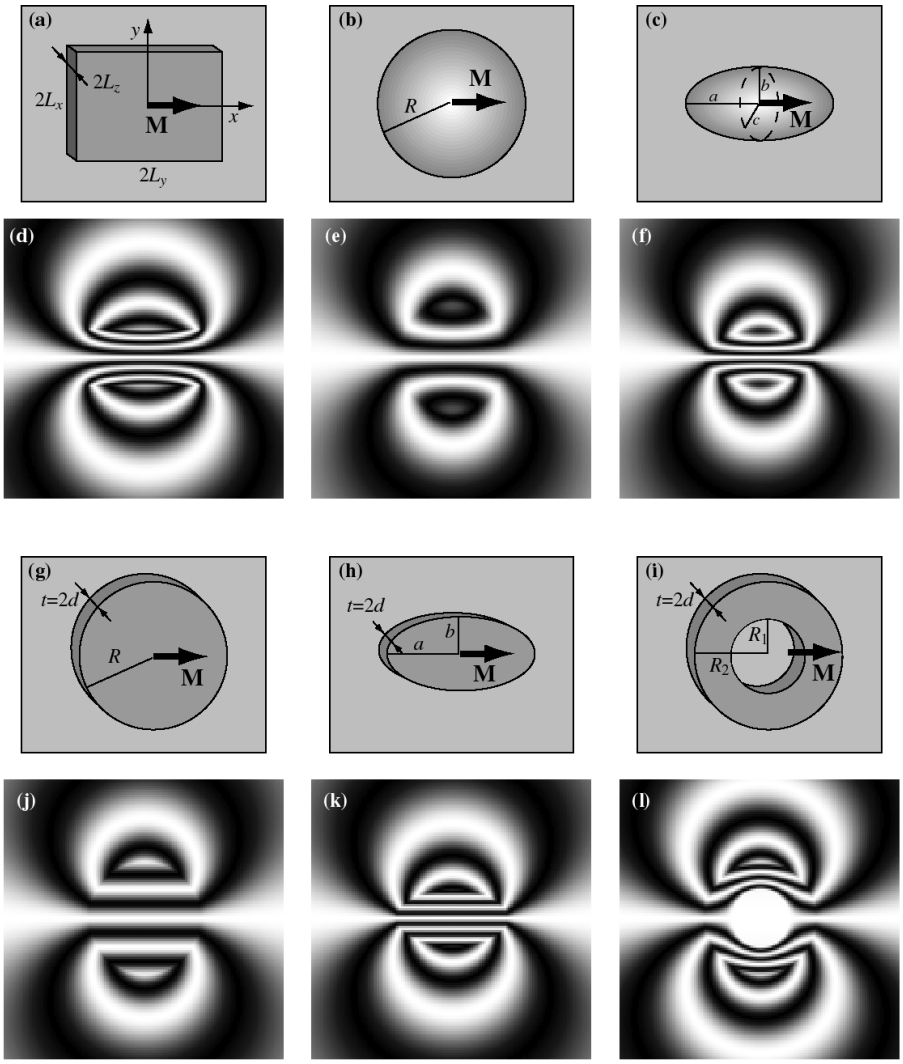

Figure 11: (a-c,g-i): basic shapes considered; (d-f,j-l): phase shift, displayed as cosine map, associated to each of the basic shapes magnetized along the x-axis.

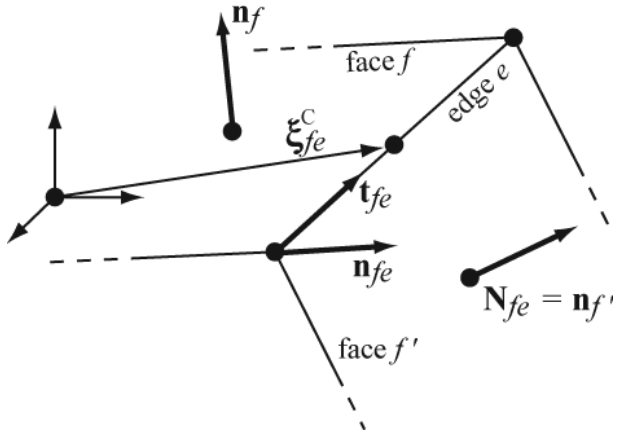

Figure 12: Schematic representation of the face normals $\mathbf{n}_f$, edge vectors $\mathbf{t}_{fe}$ and outward edge normals $\mathbf{n}_{fe}$ used in equation (46).

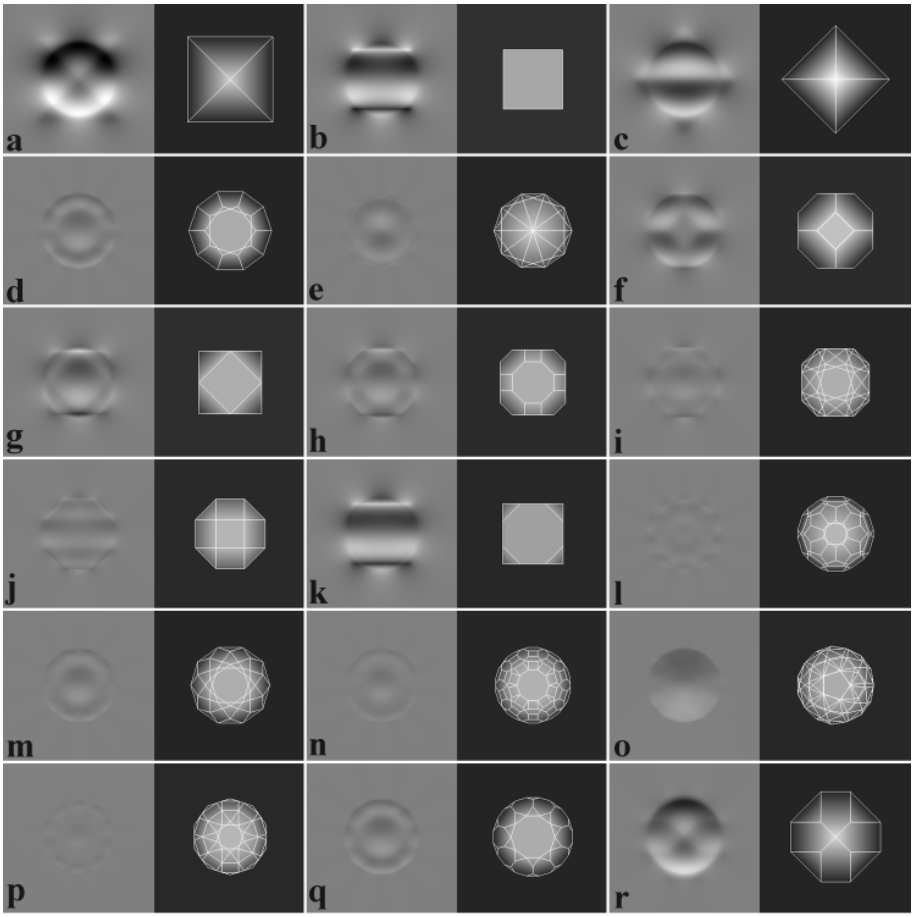

Figure 13: Magnetic and electrostatic phase shifts for the 5 Platonic and 13 Archimedean shapes. All particles have identical volumes (10^6 nm^3). The magnetic phase shifts are divided by the phase shift for an equal volume sphere with the same magnetization. The projected edge drawing of each polyhedron is superimposed on the electrostatic phase shift. (ar) refer to the entries in the last column of table 1.

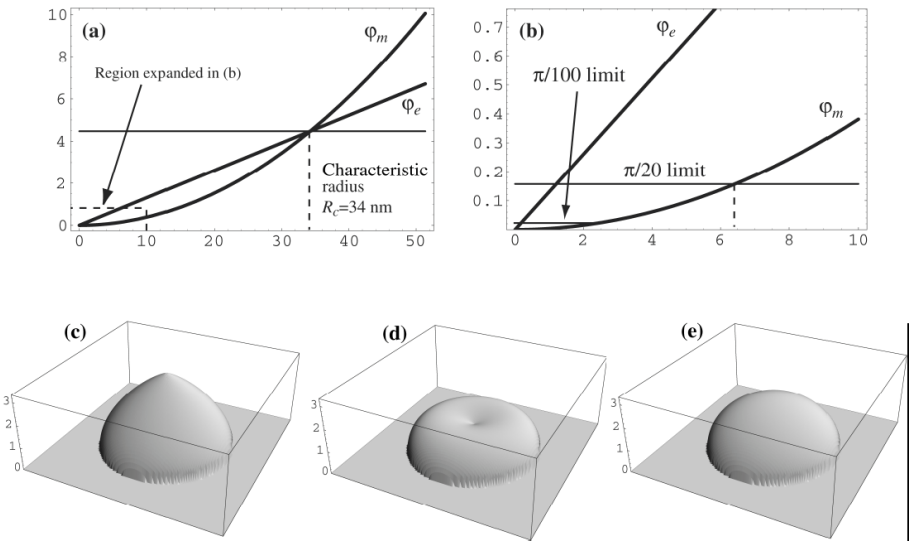

Figure 14: (a) Comparison between the electrostatic and magnetic components of the phase shift in a spherical particle; (b) expansion of the region around $R = 0$ to emphasize the detectability limits; (c) total phase shift, clockwise magnetization; (d) total phase shift, counterclockwise magnetization; (e) electrostatic component of the phase shift for a spherical particle of radius $R = R_c/2 = 17$ nm.